


PAPER

[View Article Online](#)
[View Journal](#) | [View Issue](#)Cite this: *RSC Adv.*, 2019, 9, 21302

Subtle structural variation in azine/imine derivatives controls Zn^{2+} sensitivity: ESIPT-CHEF combination for nano-molar detection of Zn^{2+} with DFT support†

Somnath Khanra, Sabyasachi Ta, Milan Ghosh, Sudeshna Chatterjee and Debasis Das *

Excited-state intra-molecular proton transfer (ESIPT)-active imine and azine derivatives, structurally characterised by XRD, and denoted **L1**, **L2**, **L3** and **L4**, possess weak fluorescence. The interaction of these probes with Zn^{2+} turns ON the fluorescence to allow its nano-molar detection. Among the four ESIPT-active molecules, **L2**, **L3** and **L4** are bis-imine derivatives while **L1** is a mono-imine derivative. Among the three bis-imine derivatives, one is symmetric (**L3**) while **L2** and **L4** are unsymmetrical. The lowest detection limits (DL) of **L1**, **L2**, **L3** and **L4** for Zn^{2+} are 32.66 nM, 36.16 nM, 15.20 nM and 33.50 nM respectively. All the probes bind Zn^{2+} (10^5 M^{-1} order) strongly. Computational studies explore the orbital level interactions responsible for the associated photo-physical processes.

Received 15th May 2019
Accepted 30th June 2019

DOI: 10.1039/c9ra03652k

rsc.li/rsc-advances

Introduction

Design and development of organic molecules for selective recognition of bio-relevant metal ions is a vibrant field of research for its extensive application in biology, ecology and endocrine systems.^{1–6} Meanwhile, the concept of excited-state intra-molecular proton transfer (ESIPT) processes has been extensively applied in molecular probes, luminescent materials, and molecular logic gates as it offers large Stokes shifts⁷ to exclude spectral overlap between absorption and emission, highly desirable for fluorescence sensing.^{8–10} The basis of ESIPT is an intra-molecular hydrogen bond that allows proton transfer from a relatively acidic region of a molecule (hydrogen bond donor, $-\text{OH}$ and NH_2) to its basic region (hydrogen bond acceptor, $=\text{N}-$ and $\text{C}=\text{O}$), leading to formation of a five/six membered ring. In most cases, this happens due to the existence of keto-enol tautomerism in the system. In some cases, this leads to dual fluorescence, one at a shorter wavelength due to the enol form and the other at a longer wavelength due to the proton-transferred form.¹¹ Knocking out this proton by a cation arrests this ESIPT process, leading to fluorescence enhancement.

The importance of biological zinc needs no introduction.^{12,13} In humans, its concentration varies from 12 μM (intracellular serum) to ~ 0.1 – 0.5 mM (brain and nerve tissue).¹⁴ As Zn^{2+} strongly interacts

with proteins,¹⁵ peptides and enzymes,^{16,17} it regulates functions like gene expression, cellular metabolism, apoptosis, neurotransmission, mammalian reproduction and so on. Moreover, zinc disorders directly affect the metabolic activities of DNA.^{18–21} The US Food and Nutritional Board recommends a daily dietary intake of Zn^{2+} from 2 mg (infants, 0–5 years) to 15 mg for adults.²² Its deficiency reduces the ability of the islet cells to produce insulin.²³ Excess Zn^{2+} is neurotoxic and can cause serious neurological disorders like Alzheimer's and Parkinson's disease.^{24–30} The WHO recommends up to 76 μM Zn^{2+} in drinking water.^{31,32} Among a significant number of pioneering Zn^{2+} sensors,^{33–36} a few recent reports deserve to be mentioned here. For example, Yoon *et al.*³⁷ developed both *R* and *S* forms of a bis-binaphthol-pyrene conjugate for selective recognition of Zn^{2+} . Bhalla *et al.*³⁸ have reported a hexaphenylbenzene derivative to recognise Zn^{2+} in aqueous media. Out of several notable efforts at Zn^{2+} sensing,^{39,40} however, few are based on the ESIPT approach.^{41,42}

Herein, an imine (**L1**) and three azine (**L2**, **L3** and **L4**) derivatives have been synthesised and structurally characterised by single crystal X-ray diffraction analysis. Out of the three azine derivatives, one is symmetrical (**L3**) while other two (**L2** and **L4**) are unsymmetrical. Photo-physical interactions of all the molecules with Zn^{2+} allow selective determination of nano-molar Zn^{2+} .

Experimental

Materials and equipment

High purity bis-tris buffer, 4-diethylamino-2-hydroxy-benzaldehyde, *N*¹-phenyl-ethane-1,2-diamine, 2-hydroxy benzaldehyde, 4-methoxy benzaldehyde, 4-hydroxy benzaldehyde, $\text{Zn}(\text{OAc})_2$, ZnCl_2 , ZnSO_4 , $\text{Zn}(\text{PO}_4)_3$, $\text{Zn}(\text{OCl})_2$ and other

Department of Chemistry, The University of Burdwan, Golapbag, Burdwan, 713104, West Bengal, India. E-mail: ddas100in@yahoo.com; Fax: +91-342-2530452; Tel: +91-342-2533913 ext. 424

† Electronic supplementary information (ESI) available: NMR, FTIR, UV-Vis, fluorescence spectra, X-ray single crystal data and DFT calculation data. CCDC 1484206, 1062760 and 1501269. For ESI and crystallographic data in CIF or other electronic format see DOI: 10.1039/c9ra03652k



chemicals have been purchased from Sigma-Aldrich (India) and used as received. The spectroscopic and analytical grade solvents were used without further purification. Milli-Q Millipore 18.2 MΩ cm⁻¹ water was used as and when required.

Absorption spectra were recorded with a Shimadzu Multi Spec 2450 spectrophotometer. A Hitachi F-4500 spectrofluorometer was used to record steady state emission spectra. The elemental analyses (C, H and N) have been performed on a PerkinElmer 2400 CHN elemental analyser. FTIR spectra were collected using a Shimadzu FTIR (model IR Prestige 21 CE) spectrometer. Electrospray ionisation mass spectra (ESI mass) were recorded using a Thermo Fisher Scientific Exactive Mass Spectrometer using HR (+/-) mode. The pH was measured using a Systronics digital pH meter (model 335). The ¹H NMR spectra were collected using a Bruker 400 MHz spectrometer using CDCl₃ and DMSO-d₆ as solvent. The chemical shift is expressed in ppm using the residual solvent peak as an internal reference. Multiplicity is indicated as follows: s (singlet), d (doublet), t (triplet), q (quartet), m (multiplet). Coupling constants (*J*) are reported in Hertz (Hz).

Single crystal X-ray diffraction data were collected on a Bruker X8 APEX-II CCD diffractometer at 100(2) K using graphite-monochromated Mo-K_α radiation (0.71073 Å) at 150 K. Data were processed and corrected for Lorentz and polarisation absorption effects. Crystal structures were solved by standard direct methods using SHELXS⁴³ and refined by full-matrix least-squares with SHELXL⁴⁴ and OLEX2 software.⁴⁵ Significant crystal parameters and refinement data are presented in Table S1 (ESI[†]). All non-hydrogen atoms are refined with anisotropic thermal displacements. Hydrogen atoms are included in the structure factor calculation in geometrically idealised positions, with thermal parameters depending on the parent atom, using a riding model. Images were generated by Mercury software.⁴⁶

Synthesis

Fig. 1 shows the molecules (L1, L2, L3 and L4) that have been synthesised simply by refluxing mixtures of aldehyde and amine (1 : 1 or 1 : 2, mole ratio) as per requirement.

5-Diethylamino-2-[(2-phenylamino-ethylimino)-methyl]-phenol (L1). A mixture of 4-diethylamino-2-hydroxy-benzaldehyde (80.876 mg, 0.41 mmol) and *N*¹-phenyl-ethane-1,2-diamine (57 mg, 0.41 mmol) in methanol was refluxed for ~4 h (Scheme 1). Slow evaporation of the solvent resulted in yellow crystals of L1 in 94.5% yield. Molecular

formula, C₁₉H₂₅N₃O (MW, 311.20). Anal. found (%): C, 73.08; H, 7.69 and N, 12.89; calcd (%), C, 73.28; H, 8.09 and N, 13.49. ESI-MS (*m/z*): [M + H]⁺, 312.32; [M + Na]⁺, 334.32 [Fig. S1a, ESI[†]]. FTIR (KBr, cm⁻¹): 3370, ν(O-H); 3038, ν(C-H, aromatic); 1608, ν(C=N); 1512, ν(C=C, stretch); 1331, ν(C-N, stretch) 1250 and 1144, ν(C-O, stretch); [Fig. S1b, ESI[†]]. ¹H NMR (CDCl₃, 400 MHz, *J*, Hz, δ ppm, reference peak 7.26 ppm) [Fig. S1c, ESI[†]]: 10.730 (1H, s) 9.499 (1H, s), 8.224 (1H, s) 7.970 (1H, s), 7.276 (1H, s), 7.205–7.160 (2H, m), 6.987–6.965 (1H, d, *J* = 8.8 Hz) 6.736–6.700 (1H, q), 6.643–6.614 (1H, m), 6.181–6.134 (1H, m), 3.715–3.687 (1H, t, *J* = 5.6 Hz), 3.571–3.541 (1H, t, *J* = 6.0 Hz), 3.490–3.317 (3H, m), 1.288–1.213 (1H, q), 1.204–1.158 (2H, m). The structure of L1 was confirmed by SC-XRD analysis.

1-[(4-Methoxy-benzylidene)-hydrazonomethyl]-naphthalen-2-ol (L2). First, 1-hydrazonomethyl-naphthalen-2-ol was synthesised following a published procedure.⁴⁷ This new amine (61 mg, 0.35 mmol) and 4-methoxy-benzaldehyde (48 mg, 0.35 mmol) were mixed in 1 : 1 mole ratio and refluxed for 4 h (Scheme 1). The final solution was kept for slow evaporation and yellow crystals of L2 were collected after one week in 91% yield. Molecular formula: C₁₉H₁₆N₂O₂ (MW = 304.12). Anal. found (%), C, 74.78; H, 5.11 and N, 9.39; calcd (%), C, 74.98; H, 5.30 and N, 9.20. ESI-MS (*m/z*): [M + H]⁺, 305.29; [M + Na]⁺, 327.28 [Fig. S2a, ESI[†]]. FTIR (KBr, cm⁻¹): 3214.83, ν(O-H); 3012.81 and 2923.69, ν(C-H, aromatic); 1612.19, ν(C=N); 1507.98, ν(C=C, stretch); 1246.49 and 1172.28, ν(C-O, stretch); 1098.13, ν(N-N, stretch). [Fig. S2b, ESI[†]]. ¹H NMR (CDCl₃, 400 MHz, *J*, Hz, δ ppm, reference peak, 7.26 ppm) [Fig. S2c, ESI[†]]: 13.406 (1H, s), 9.707 (1H, s), 9.646 (1H, s), 8.740–8.634 (1H, d, *J* = 1.6 Hz), 8.574 (1H, s), 8.202–8.181 (2H, d, *J* = 8.4 Hz), 7.879–

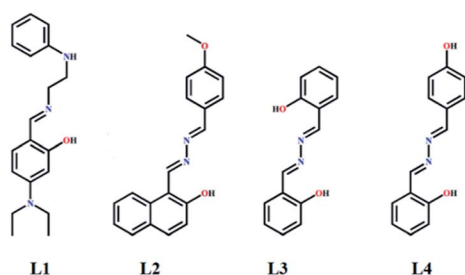
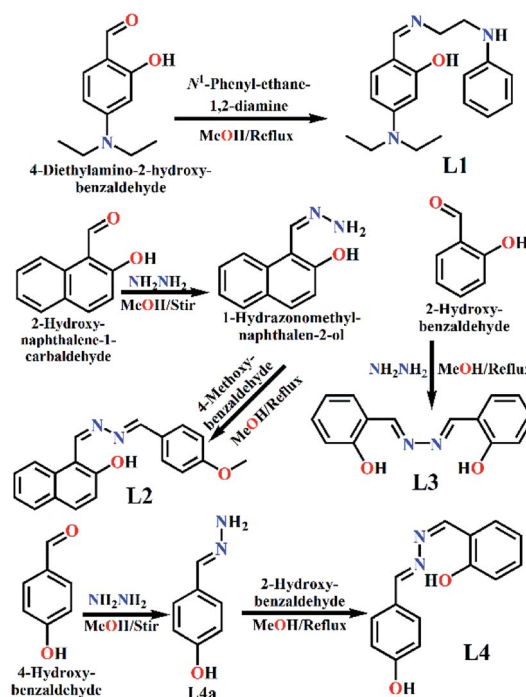


Fig. 1 ChemDraw structures of new molecules.



Scheme 1 Synthetic protocol of L1, L2, L3 and L4.



7.808 (5H, m), 7.585–7.567 (1H, d, $J = 7.2$), 7.430–7.396 (1H, d, $J = 6.4$ Hz), 7.283–7.261 (1H, d, $J = 9.2$), 7.032–7.003 (3H, t, $J = 5.8$ Hz), 3.902–3.842 (5H, t, $J = 12$ Hz). The structure of **L2** was confirmed by SC-XRD analysis.

***N,N'*-Bis-(2-hydroxy-benzylidene)-hydrazine (**L3**)**. To a methanol solution of 2-hydroxy-benzaldehyde (122 mg, 1 mmol), a slight excess of hydrazine was added and refluxed for 4 h (Scheme 1). Finally, the solution was kept for slow evaporation and yellow crystals of **L3** were collected after one week in 96.3% yield. Molecular formula: $C_{14}H_{12}N_2O_2$ (MW = 204.09). Anal. found (%), C, 69.48; H, 4.80 and N, 11.37; calcd (%), C, 69.99; H, 5.03 and N, 11.66. ESI-MS (m/z): $[M + H_2O]^+$, 257.22 (100%; calcd 258.10) [Fig. S3a, ESI†]. FTIR (KBr, cm^{-1}): 3373.91, $\nu(O-H)$; 3030.25, $\nu(C-H, \text{aromatic})$; 1597.11, $\nu(C=N)$; 1474.46, $\nu(C=C, \text{stretch})$; 1251.60, $\nu(C-O, \text{stretch})$; 1122.08, $\nu(N-N, \text{stretch})$. [Fig. S3b, ESI†]. 1H NMR (DMSO- d_6 , 400 MHz, J , Hz, δ ppm, reference peak, 2.5 ppm) [Fig. S3c, ESI†]: 10.450 (1H, s), 7.930 (1H, s), 7.203–7.179 (1H, q), 7.130–7.091 (1H, q), 6.825–6.789 (3H, t, $J = 7.2$ Hz). The structure of **L3** was further confirmed by SC-XRD analysis.

***N*-(2-Hydroxy-benzylidene)-*N'*-(4-hydroxy-benzylidene)-hydrazine (**L4**)**. Methanol solution of 4-hydroxy-benzaldehyde (122 mg, 1 mmol) was added drop-wise to hydrazine with continuous stirring to get 4-hydrazonomethyl-phenol (**L4a**) in 84.3% yield (Scheme 1). Molecular formula: $C_7H_8N_2O$ (MW, 136.06). Anal. found (%), C, 61.38; H, 5.80 and N, 19.97; calcd (%), C, 61.75; H, 5.29, N, 20.58. ESI-MS (m/z): $[M + H]^+$, 136.49 (100%; calcd 137.07) [Fig. S4a, ESI†]. FTIR (KBr, cm^{-1}): 3481.02, $\nu(N-H)$; 3316.83, $\nu(O-H)$; 3176.50, $\nu(C-H, \text{aromatic})$; 1600.97, $\nu(C=N)$; 1508.14, $\nu(C=C, \text{stretch})$; 1253.26 and 1158.12, $\nu(C-O, \text{stretch})$; 1100.24, $\nu(N-N, \text{stretch})$. [Fig. S4b, ESI†]. 1H NMR (DMSO- d_6 , 400 MHz, J , Hz, δ ppm, reference peak, 2.5 ppm) [Fig. S4c, ESI†]: 10.726 (1H, s), 9.500 (2H, s), 8.547 (1H, s), 7.693–7.671 (2H, d, $J = 8.8$ Hz), 7.615 (1H, s), 7.305–7.278 (2H, q), 6.863–6.842 (2H, d, $J = 8.4$ Hz), 6.725–6.704 (2H, q), 6.369 (2H, s).

Then **L4** was synthesised by refluxing a mixture of **L4a** (68 mg, 0.5 mmol) and 2-hydroxy-benzaldehyde (61 mg, 0.5 mmol) in methanol for 3 h (Scheme 1). The final solution was kept for slow evaporation and yellow crystals of **L4** were observed after one week in 92.7% yield. Molecular formula: $C_{14}H_{12}N_2O_2$ (MW, 240.09). Anal. found (%), C, 70.12; H, 4.83 and N, 11.02; calcd (%), C, 69.99; H, 5.03 and N, 11.66. ESI-MS (m/z): $[M + H]^+$, 241.79 [Fig. S4d, ESI†]. FTIR (KBr, cm^{-1}): 3319.09, $\nu(O-H)$; 3027.96, $\nu(C-H, \text{aromatic})$; 1616.41, $\nu(C=N)$; 1478.60, $\nu(C=C, \text{stretch})$; 1216.17 and 1154.94, $\nu(C-O, \text{stretch})$; 1100.71, $\nu(N-N, \text{stretch})$. [Fig. S4e, ESI†]. 1H NMR (DMSO- d_6 , 400 MHz, J , Hz, δ ppm, reference peak, 2.5 ppm) [Fig. S4f, ESI†]: 11.427 (1H, s), 11.051 (1H, s), 8.993 (1H, s), 7.940 (1H, s), 7.696–7.677 (1H, d, $J = 7.6$ Hz), 7.418–7.379 (1H, t, $J = 7.8$ Hz), 7.222–7.203 (1H, t, $J = 3.8$), 7.155–7.009 (1H, q), 6.997–6.907 (2H, m), 6.873–6.804 (4H, m).

[Probe- Zn^{2+}] adducts (Ad1**, **Ad2**, **Ad3** and **Ad4**)**. To four sets of magnetically stirred methanol solutions of **L1**, **L2**, **L3** and **L4**, methanol solutions of $Zn(OAc)_2$ were added drop-wise for 10–15 min. After filtration, the filtrate was kept for slow evaporation

and yellow-white solids corresponding to the adducts, viz. **L1**- $Zn(OAc)_2$ (**Ad1**), **L2**- $Zn(OAc)_2$ (**Ad2**), **L3**- $Zn(OAc)_2$ (**Ad3**), and **L4**- $Zn(OAc)_2$ (**Ad4**), were found after two days (Fig. 5).

Ad1: molecular formula, $C_{21}H_{27}N_3O_3Zn$; anal. found (%), C, 57.41; H, 6.17 and N, 8.30; calcd (%), C, 58.00; H, 6.26 and N, 9.66. ESI-MS (m/z): $[Ad1 + MeOH + Na]^+$, 486.79 [Fig. S5a, ESI†]. FTIR (KBr, cm^{-1}): 3107.81, $\nu(C-H, \text{aromatic})$; 1560.60, $\nu(C=N)$; 1437.17, $\nu(C=C, \text{stretch})$; 1247.28 and 1148.75, $\nu(C-O, \text{stretch})$ [Fig. S5b, ESI†].

Ad2: molecular formula, $C_{21}H_{19}N_2O_4Zn$; anal. found (%), C, 58.41; H, 5.07 and N, 6.01; calcd (%), C, 58.82; H, 4.47 and N, 6.53. ESI-MS (m/z): $[M + Na]^+$, 451.50 [Fig. S6a, ESI†]. FTIR (KBr, cm^{-1}): 3102.54, $\nu(C-H, \text{aromatic})$; 1557.86, $\nu(C=N)$; 1451.65, $\nu(C=C, \text{stretch})$; 1249.97 and 1169.97, $\nu(C-O, \text{stretch})$; 1066.20, $\nu(N-N, \text{stretch})$ [Fig. S6b, ESI†].

Ad3: molecular formula, $C_{18}H_{18}N_2O_6Zn_2$; anal. found (%), C, 43.68; H, 4.23 and N, 4.97; calcd (%), C, 44.20; H, 3.71 and N, 5.73. ESI-MS (m/z): $[M + H]^+$, 486.18 [Fig. S7a, ESI†]. FTIR (KBr, cm^{-1}): 3098.60, $\nu(C-H, \text{aromatic})$; 1601.91 and 1574.94, $\nu(C=N)$; 1438.32, $\nu(C=C, \text{stretch})$; 1312.55 and 1171.95, $\nu(C-O, \text{stretch})$; 1135.28, $\nu(N-N, \text{stretch})$ [Fig. S7b, ESI†].

Ad4: molecular formula, $C_{16}H_{15}N_2O_4Zn$; anal. found (%), C, 52.85; H, 3.92 and N, 6.76; calcd (%), C, 52.69; H, 4.15 and N, 7.68. ESI-MS (m/z): $[M + H]^+$, 363.07 [Fig. S8a, ESI†]. FTIR (KBr, cm^{-1}): 3102.54, $\nu(C-H, \text{aromatic})$; 1614.49 and 1559.52, $\nu(C=N)$; 1450.67, $\nu(C=C, \text{stretch})$; 1286.86 and 1197.53, $\nu(C-O, \text{stretch})$; 1111.63, $\nu(N-N, \text{stretch})$. [Fig. S8b, ESI†].

Results and discussion

Single crystal X-ray diffraction analysis of **L1**, **L2** and **L3**

L1, **L2** and **L3** were well characterised by spectroscopic techniques and their stereo-chemical structures were confirmed by single crystal X-ray diffraction analysis (Fig. 2). Their molecular views along with atom labelling schemes are shown in Fig. S9a–c (ESI†) while their packing patterns are shown in Fig. S10a–c (ESI†). The crystallographic data and refinement parameters are presented in Table S1 (ESI†) while selected bond lengths and angles are listed in Table S2a–c (ESI†).

L1 is triclinic having space group $P\bar{1}$ (CCDC 1484206): a , 10.8682(5) (Å); b , 11.1818(6) (Å); c , 16.0637(8) (Å); α (°), 88.542(3); β (°), 73.254(2); γ (°), 70.084(3); volume (Å³), 1754.84(15); $Z = 4$ (Table S1 (ESI†)). It exists as the enol form in the solid state. The bond lengths N003–C00J, 1.322(2) Å and N005–C00H, 1.295(2) Å indicate the double bond character of C–N whereas N004–C00Z, 1.447(3) Å, N004–C00W, 1.462(2) Å, N3–C00Q, 1.448(3) Å, and N3–C016, 1.536(4) Å indicate the single bond character of C–N bonds in the *N*-ethyl amino group. The bond lengths O001–C00C, 1.305(2) Å and O002–C00M, 1.291(2) Å indicate the single bond character of C–O in the phenol moiety. The structure is stabilised by intra-molecular H-bonding. The bond angles C00J–N003–C00V, 121.68(18)° and C00H–N005–C00T, 124.16(16)° indicate the sp^2 nature of the N003 and N005 centres (Fig. S9a and Table S2a, ESI†).

L2 is monoclinic having space group $P\bar{1}$ (CCDC 1062760): a , 7.1822(10) (Å); b , 14.0258(18) (Å); c , 15.7770(19) (Å); α (°), 89.987(9); β (°), 90.007(10); γ (°), 77.128(10); volume (Å³),



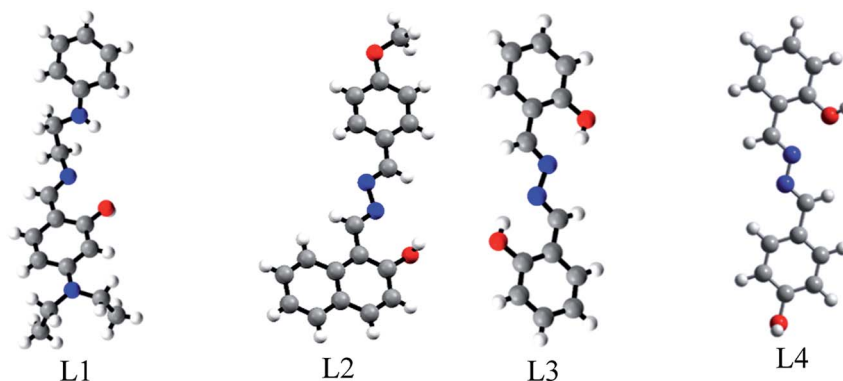


Fig. 2 ORTEP views of L1, L2 and L3 and DFT optimised structure of L4.

1549.4(4); $Z = 4$ (Table S1, ESI[†]). It exists as the enol form in the solid state. The bond lengths N007–C00I, 1.284(6) Å and N003–C00R, 1.288(6) Å indicate the double bond character of C–N of the aldimine group whereas N006–C00D, 1.280(6) Å and N008–C00T, 1.279(6) Å indicate the C–N bond on the *p*-methoxy benzaldehyde side. The bond lengths N003–N006, 1.405(6) Å and N007–N008, 1.403(6) Å indicate the single bond character of N–N from the hydrazine moiety. The bond lengths O1–C00J, 1.347(6) Å and O2–C00K, 1.348(6) Å indicate the single bond character of C–O in the phenol moiety. The structure is stabilised by intra-molecular H bonding. The bond angles C00R–N003–N006, 114.2(5)°, C00D–N006–N003, 113.0(5)°, C00I–N007–N008, 113.6(5)°, and C00T–N008–N007, 112.7(5)° indicate the sp^2 nature of the N003, N006, N007 and N008 centres (Fig. S9b and Table S2b, ESI[†]).

L3 is monoclinic having space group $P2_1/c$ (CCDC 1501269): a , 16.524(3) (Å); b , 5.9394(12) (Å); c , 13.232(2) (Å); α (°), 90; β (°), 113.560(11); γ (°), 90; volume (Å³), 1190.4(4); $Z = 4$ (Table S1, ESI[†]). It exists as the enol form in the solid state. The bond lengths N2–C14, 1.277(7) Å and N1–C7, 1.286(7) Å indicate the double bond character in C–N of the aldimine group whereas N004–C00Z, 1.447(3) Å, N1–N1, 1.395(9) Å and N2–N2, 1.409(9) Å indicate the single bond character of N–N in the hydrazine moiety. The bond lengths O1–C1, 1.356(7) Å and O2–C8, 1.350(7) Å indicate the single bond character of C–O in the phenol moiety. The structure is stabilised by intra-molecular H bonding. The bond angles C14–N2–N2, 113.3(6)°, N2–C14–C13, 121.7(6)°, C7–N1–N1, 113.1(6)°, and N1–C7–C6, 121.3(6)° indicate the sp^2 nature of the N003, N006, N007 and N008 centres (Fig. S9c and Table S2c, ESI[†]).

Spectroscopic studies

Emission properties. The presence of both acidic (–OH) and basic (NHR and –C=NR) moieties makes L1, L2, L3 and L4 pH sensitive. Consequently, their emission properties upon interaction with cations, anions and biomolecules have been investigated at different pH. Interestingly, their weak emission (L1: λ_{em} , 414 nm, λ_{ex} , 287 nm; L2: λ_{em} , 491 nm, λ_{ex} , 436 nm; L3: λ_{em} , 431 nm, λ_{ex} , 353 nm and L4: λ_{em} , 495 nm, λ_{ex} , 400 nm) is enhanced significantly in the presence of Zn^{2+} : specifically, the enhancement is maximum for $Zn(OAc)_2$. Other common metal

ions, *viz.* Na^+ , K^+ , Ca^{2+} , Al^{3+} , Hg^{2+} , Pb^{2+} , Cr^{3+} , Mn^{2+} , Fe^{3+} , Co^{2+} , Ni^{2+} , Cu^{2+} , Cd^{2+} , Sn^{2+} and Ag^+ , do not significantly affect their emission intensities (Fig. 3a–d). Moreover, Zn salts other than $Zn(OAc)_2$, *viz.* $ZnCl_2$, $ZnSO_4$, $Zn(PO_4)_3$, and $Zn(OC)_2$, show similar fluorescence enhancements in response to Zn^{2+} . In addition, the emission intensity of L1– $Zn(OAc)_2$ (Ad1) is maximum over the pH range 7 to 10 (Fig. S11a–d, ESI[†]). Hence, the near-biological pH 7.4 was chosen for all experiments. As L1 emits at two different wavelengths, a ratiometric change is observed upon gradual addition of $Zn(OAc)_2$ to L1.

The emission intensity decreases at 316 nm while it increases at 414 nm through an iso-emissive point at 371 nm (Fig. 4a). In all other cases (excluding L1), the emission intensity at the respective wavelength increases upon gradual addition of $Zn(OAc)_2$ (for L2, 491 nm, for L3, 431 nm and for L4, 495 nm) (Fig. 4b–d). Competitive experiments indicate no significant interference from common metal ions during sensing of Zn^{2+} in the form of $Zn(OAc)_2$ by L1–L4 (Fig. S12a–d, ESI[†]). The change in emission intensities of L1 at two different wavelengths (414 nm and 316 nm) upon addition of Zn^{2+} is shown in Fig. S13a (ESI[†]). Similar plots for L2, L3 and L4 are shown in Fig. S13b–d (ESI[†]). The linear regions of the plots allow determination of unknown concentrations of Zn^{2+} . The lowest detection limits (DL) of Zn^{2+} by L1, L2, L3 and L4 are 32.66 nM, 36.16 nM, 15.20 nM and 33.50 nM respectively (Fig. S14a–d, ESI[†]). These values lie well below the WHO recommended acceptable level of Zn^{2+} in drinking water (76 μ M). The DL of L3 for Zn^{2+} is the lowest in the series, indicating stronger interaction of L3 with Zn^{2+} , probably due to the presence of two –OH groups. Fluorescence titration enables determination of the association constants (K) of the probes for Zn^{2+} using the Benesi–Hildebrand equation (Fig. S15a–d, ESI[†]).

The respective association constants are $2.146 \times 10^5 M^{-1}$, $2.407 \times 10^5 M^{-1}$, $3.28 \times 10^5 M^{-2}$ and $1.692 \times 10^5 M^{-1}$ for L1, L2, L3 and L4 respectively. The fact that L3 has the highest K is due to the same reason as its having the lowest DL. From the Job plots (Fig. S16a–d, ESI[†]), ESI mass spectra (Fig. S5a, S6a, S7a and S8a, ESI[†]), FTIR spectra (Fig. S5b, S6b, S7b and S8b, ESI[†]), and 1H NMR titration (Fig. 7), plausible binding modes of L1–L4 with Zn^{2+} are proposed in Scheme 2 and the corresponding adducts (Ad1–Ad4) are presented in Fig. 5. Scheme 2 shows the



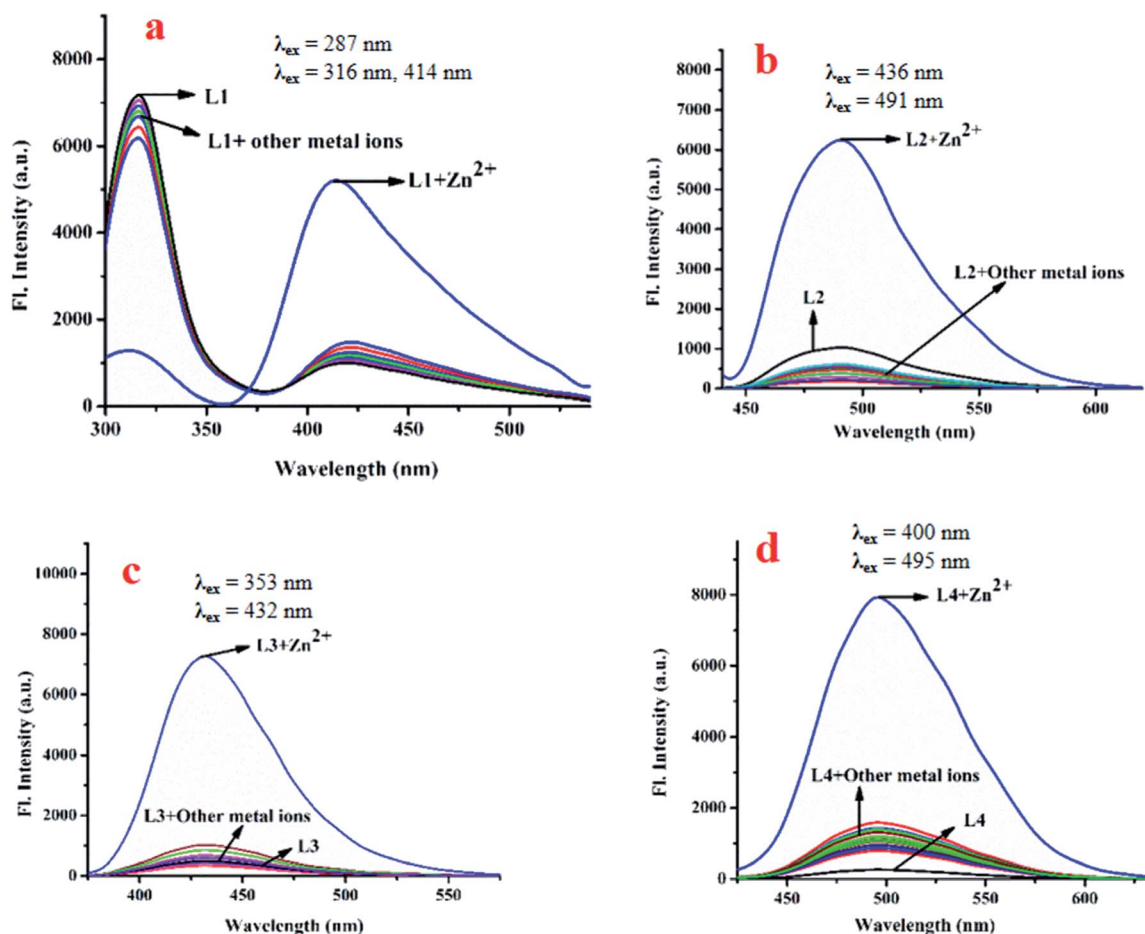


Fig. 3 Changes in the emission spectra of L1 (a), L2 (b), L3 (c) and L4 (d) in presence of different metal ions in bis-tris buffered DMSO/H₂O (1 : 1, v/v) media, pH 7.4.

probable sensing mechanism, assigned to the combined effect of ESIPT and chelation enhanced fluorescence (CHEF).

Absorption properties. The absorption spectrum of **L1** exhibits two peaks, viz. 242 nm and 363 nm, assigned to π - π^* and n - π^* transitions.⁴⁸ Upon gradual addition of Zn(OAc)₂ to **L1**, the absorbance at both wavelengths increases (Fig. 6a) while for the rest (**L2**–**L4**), a ratiometric change is observed. For **L2**, the absorbance decreases at 380 nm but increases at 439 nm through an isosbestic point at 402 nm (Fig. 6b). For **L3**, the weak absorbance at 346 nm increases while the absorbance at 308 nm decreases with the appearance of four isosbestic points at 256 nm, 279 nm, 296 nm, and 321 nm (Fig. 6c). The situation for **L4** is almost the same as that of **L2**. The absorbance at 354 nm decreases with the emergence of a new band at 404 nm through an isosbestic point at 377 nm (Fig. 6d). Changes in the absorption spectra of **L1**–**L4** in the presence of common cations are presented in Fig. S17a–d (ESI†).

Sensing mechanism

The ESI mass spectra of **Ad1**, **Ad2** and **Ad4** along with the Job plots (Fig. S16a, b and d, ESI†) support 1 : 1 (mole ratio) binding stoichiometry between the probe and Zn(OAc)₂ whereas the

corresponding data for **Ad3** indicate 1 : 2 (mole ratio) stoichiometry (Fig. S16c, ESI†). Thus chelation of **L1**–**L4** to zinc ion leads to CHEF through inhibition of ESIPT and –CH=N– isomerisation (Scheme 2 and Fig. 5). ¹H NMR titration of **L1**–**L4** with Zn(OAc)₂ further supports the proposed mechanism. The FTIR data of the adducts also corroborate the binding mode (Fig. S5b, S6b, S7b and S8b, ESI†). It was observed that the ν (C=N) band of free **L1**, **L2**, **L3** and **L4** at 1608, 1612, 1597 and 1616 cm^{−1} shifted to 1560, 1557, 1574, 1559 cm^{−1} in the respective adducts **Ad1**, **Ad2**, **Ad3** and **Ad4**, in addition to their original peaks in some cases. This indicates involvement of imine-N in chelation. Moreover, the respective ν (O–H) bands at 3370, 3214, 3373 and 3319 cm^{−1} almost disappear in the case of **Ad1**, **Ad2** and **Ad4** while it partially disappears for **Ad3**. Thus ESIPT protons disappear upon binding of phenol-O to Zn(OAc)₂.

¹H NMR titration

The ¹H NMR titration results unveil the binding mode of **L1** with Zn(OAc)₂ (Fig. 7a). Upon addition of 0.5 equiv. of Zn²⁺, the highly de-shielded proton (–OH) at 10.73 ppm almost disappears, indicating interaction of phenol-O with Zn²⁺, while the imine proton is slightly up-field shifted from 9.49 ppm to



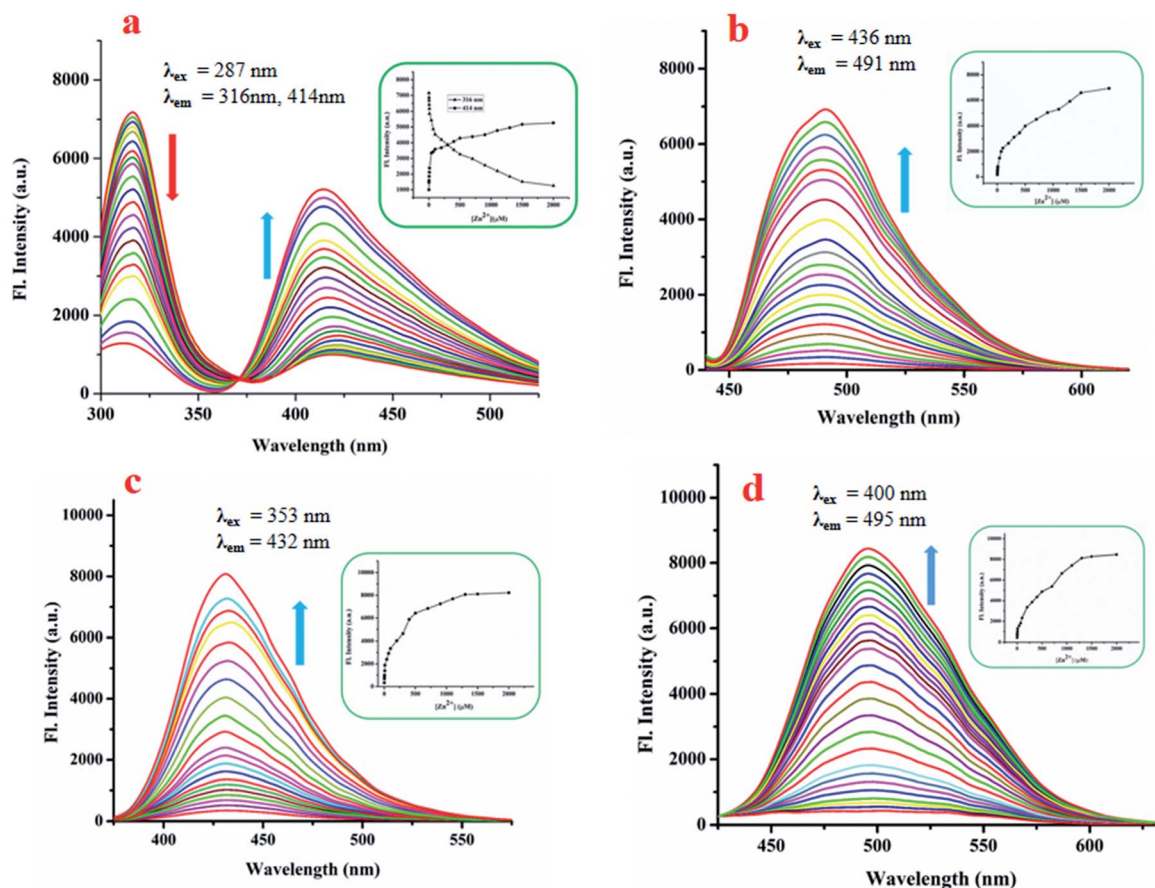
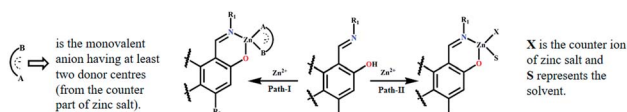


Fig. 4 Changes in emission intensity of L1 (a), L2 (b), L3 (c) and L4 (d) upon gradual addition of $\text{Zn}(\text{OAc})_2$; inset: plot of emission intensities vs. added $\text{Zn}(\text{OAc})_2$ at respective emission wavelengths. Media and pH are same as in Fig. 3.



Scheme 2 Binding mode of L1, L2, L3 and L4 towards Zn^{2+} salt.

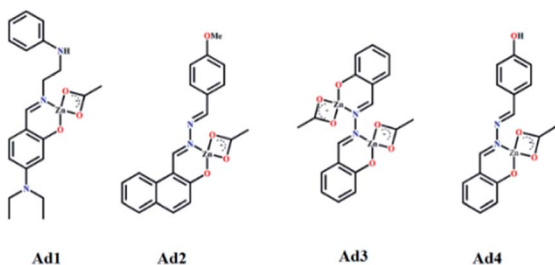


Fig. 5 Binding mode of L1, L2, L3 and L4 with $\text{Zn}(\text{OAc})_2$ forming adduct Ad1, Ad2, Ad3 and Ad4 respectively.

9.41 ppm, suggesting involvement of imine-N in chelation.⁵⁷ At 1.0 equiv. of $\text{Zn}(\text{OAc})_2$ the phenol proton completely disappears, while the imine proton is further shifted from 9.41 ppm to 9.40 ppm. Similar facts are observed for L2 and L4. In the case of

L2, the $-\text{OH}$ proton at 13.41 ppm gradually disappears upon gradual addition of $\text{Zn}(\text{OAc})_2$ while the imine proton experiences a slight up-field shift (Fig. 7b). However, upon addition of 1.0 equiv. $\text{Zn}(\text{OAc})_2$ to L3, the $-\text{OH}$ peak at 10.45 ppm does not disappear fully, probably due to the presence of two symmetric $-\text{OH}$ units that can equally interact with two molecules of $\text{Zn}(\text{OAc})_2$. Interestingly, upon addition of two equiv. of $\text{Zn}(\text{OAc})_2$, the $-\text{OH}$ peak almost disappears and the imine proton is shifted up-field (Fig. 7c). In L4, two $-\text{OH}$ protons at 11.427 and 11.051 ppm have been observed (Fig. S4f, ESI†). Upon addition of 0.5 equiv. $\text{Zn}(\text{OAc})_2$, the $-\text{OH}$ peak *ortho* to the imine group tends to disappear while the other $-\text{OH}$ at the *para* position of the other ring is slightly up-field shifted from 11.427 to 11.344 ppm. At saturation point both $-\text{OH}$ peaks almost disappear (Fig. 7d).

Density functional theoretical (DFT) studies

DFT studies have been performed using the TD-SCF/DFT/B3LYP/6-311G level of theory. Only the HOMO and LUMOs are provided to demonstrate the stability of the adducts compared to the free probes. The lowering of the HOMO–LUMO energy gaps in Ad1–Ad4 compared to free L1–L4 indicates stabilisation of the former over the latter. In each case, the oscillator strength (f^b) for the $S_0 \rightarrow S_1$ transition of the adduct increases compared



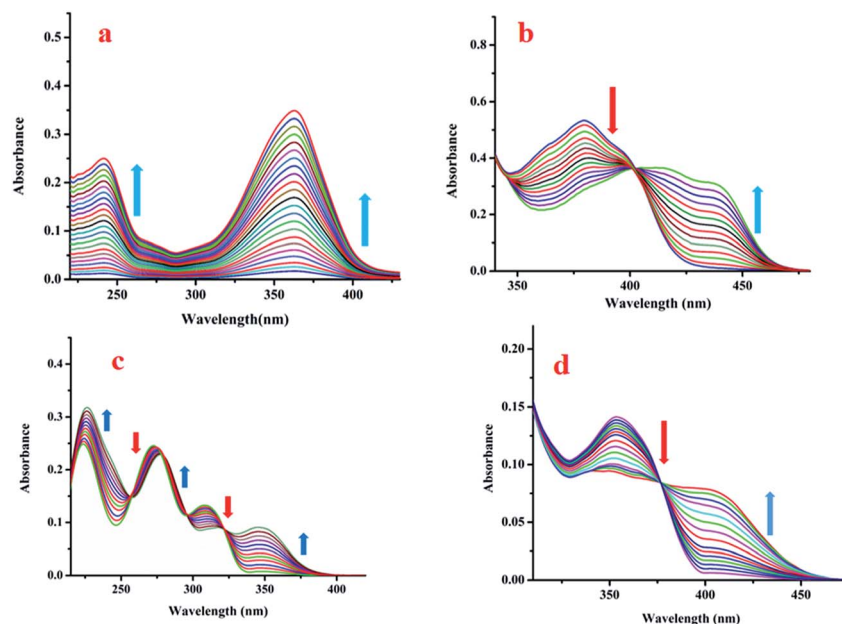


Fig. 6 Changes in the absorption spectra of (a) L1, (b) L2, (c) L3 and (d) L4 upon gradual addition of $\text{Zn}(\text{OAc})_2$.

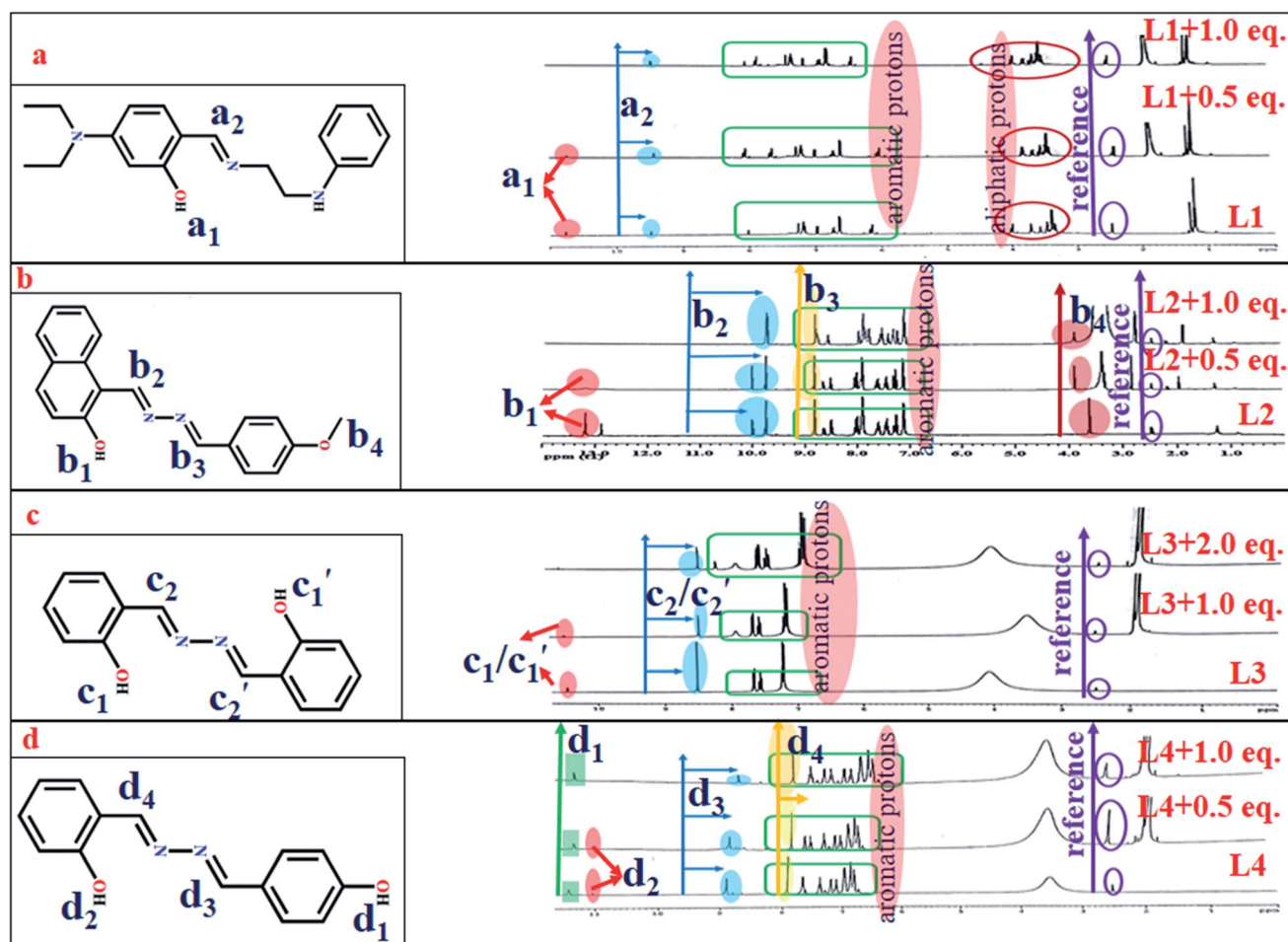


Fig. 7 ^1H NMR titration of L1 (a), L2 (b), L3 (c) and L4 (d) with $\text{Zn}(\text{OAc})_2$ in $\text{DMSO}-d_6$.



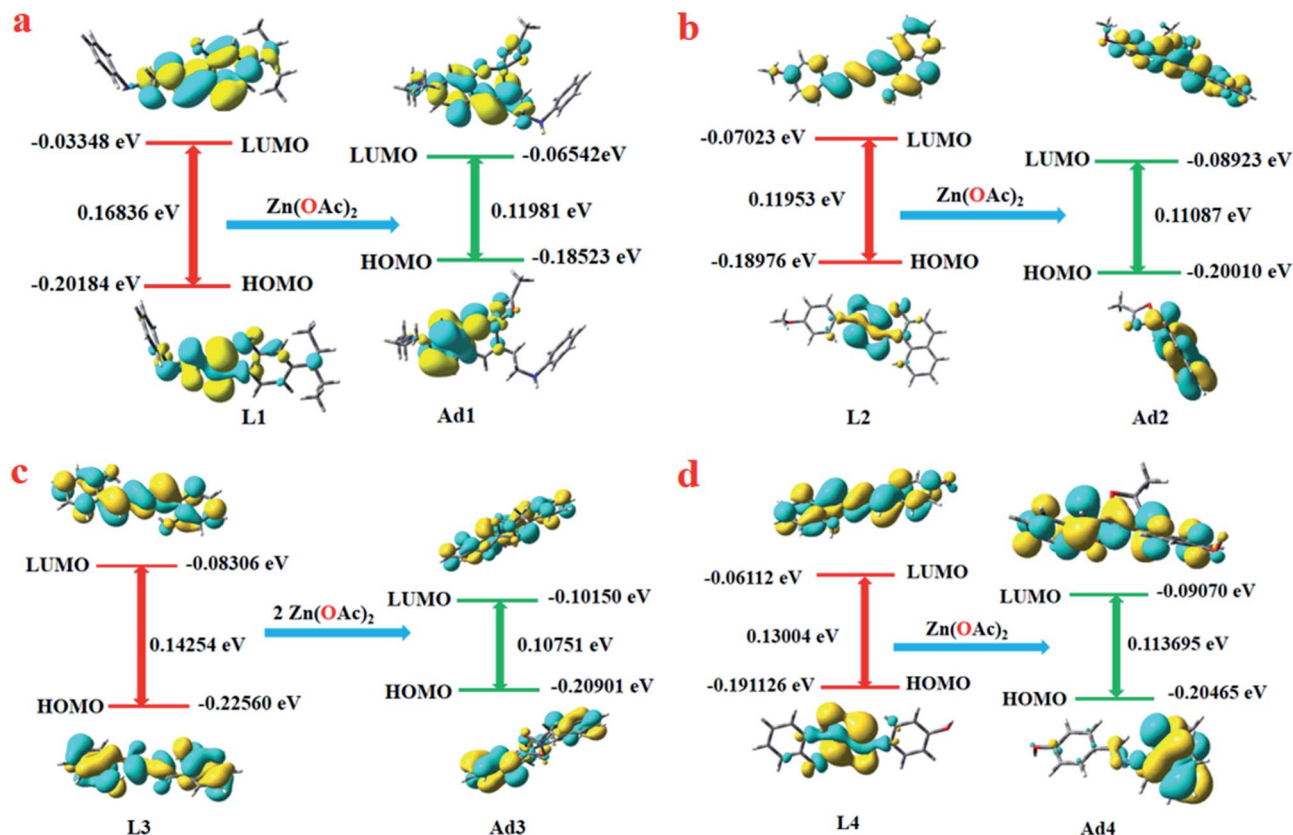


Fig. 8 Frontier molecular orbitals of L1 and its adduct Ad1 (a), L2 and its adduct Ad2 (b), L3 and its adduct Ad3 (c), and L4 and its adduct Ad4 (d).

to the free probes. This indicates increased probability of absorption/emission as observed in the experimental findings. The electron transition energies for the predominant absorption of the free probes and corresponding $\text{Zn}(\text{OAc})_2$ adducts are depicted in Table S3a–d (ESI[†]).

For **L1**, the HOMO–LUMO energy gap was reduced by 0.04855 eV from 0.16836 eV (free **L1**) to 0.11987 eV (**Ad1**) (Fig. 8a). The $S_0 \rightarrow S_1$ transition (HOMO \rightarrow LUMO) at 363 nm has a low f^b , 0.006, which indicates intra-molecular charge transfer (ICT) from phenol moieties to the amide. A hypsochromic shift to 477 nm is observed with a significant increase of f^b (0.0237) for **Ad1** ($S_0 \rightarrow S_1$ transition, HOMO \rightarrow LUMO, HOMO \rightarrow LUMO + 1), suggesting formation of rigid **Ad1**.⁴⁹ Another HOMO \rightarrow LUMO transition along with HOMO \rightarrow LUMO + 1 have been observed for $S_0 \rightarrow S_2$ with $f^b = 0.0095$. The HOMO–LUMO energy gap in **L2** is 0.11953 eV while it is 0.110807 eV in **Ad2** (Fig. 8b). Here again the main transition $S_0 \rightarrow S_1$ (HOMO \rightarrow LUMO, HOMO \rightarrow LUMO + 1) occurs with a very low value of f^b (0.0011), while **Ad2** has a higher value of f^b (0.2214) for the same electronic transition. Again one interesting observation is that the transition $S_0 \rightarrow S_2$ (HOMO – 1 \rightarrow LUMO, HOMO \rightarrow LUMO + 1, HOMO – 1 \rightarrow LUMO + 2) at 371.56 nm for **L2** is well matched with the experimental value of the absorption peak at 380 nm, and $S_0 \rightarrow S_2$ (HOMO \rightarrow LUMO, HOMO \rightarrow LUMO + 1) for **Ad2** at 430.78 nm is also well matched with the experimental value at 439 nm. We have performed a DFT study of **L3** and **Ad3**, and again observed that energy

relaxation is more pronounced in the case of **Ad3** than **L3**. The respective values of the HOMO–LUMO energy gap of **L3** and **Ad3** are 0.14254 eV and 0.10751 eV (Fig. 8c). Here also the main transition $S_0 \rightarrow S_1$ (HOMO – 1 \rightarrow LUMO, HOMO \rightarrow LUMO) occurs with a very low value of f^b (0.0032) for **L3**, as seen from the MO profile. Meanwhile, for **Ad3** the transition $S_0 \rightarrow S_1$ (HOMO – 1 \rightarrow LUMO, HOMO \rightarrow LUMO) occurs with $f^b = 0.1602$. In the case of **L4**, the HOMO–LUMO energy gap decreases from 0.13004 eV to 0.113695 eV for the **Ad4** adduct (Fig. 8d). The respective f^b values for **L4** and **Ad4** are 0.0010 and 0.0978.

Conclusion

Four simple organic molecules (Schiff base and azine derivatives) have been synthesised and structurally characterised by SC-XRD analysis. Due to the existence of an ESIPT process, a weak fluorescence is observed in the molecules. It is found that the molecules selectively interact with the Zn^{2+} ion as monitored by fluorescence and absorption spectroscopic studies. The association constants of **L1**, **L2**, **L3** and **L4** with $\text{Zn}(\text{OAc})_2$ are $2.146 \times 10^5 \text{ M}^{-1}$, $2.15 \times 10^5 \text{ M}^{-1}$, $3.28 \times 10^5 \text{ M}^{-2}$, and $1.692 \times 10^5 \text{ M}^{-1}$ respectively. The enhancement of fluorescence is due to the arrested ESIPT with the formation of a rigid adduct, leading to a CHEF process. The lowest detection limit is found to be in the nano-molar range. A DFT study elucidates the experimental results. Thus, a new class of ESIPT-



CHEF probes for recognition of Zn(II) is established for its ultra-trace level determination.

Conflicts of interest

There are no conflicts to declare.

Acknowledgements

SK and SC acknowledge CSIR, New Delhi (India) and DST-INSPIRE (India) for fellowship.

Notes and references

- 1 T. Hirano, K. Kikuchi, Y. Urano and T. Nagano, *J. Am. Chem. Soc.*, 2002, **124**, 6555–6562.
- 2 M. W. Hentze, M. U. Muckenthaler and N. C. Andrews, *Cell*, 2002, **117**, 285–297.
- 3 D. Chen, R. J. Letcher, L. T. Gauthier, S. G. Chu, R. McCrindle and D. Potter, *Environ. Sci. Technol.*, 2011, **45**, 9523–9530.
- 4 M. Vendrell, D. T. Zhai, J. C. Er and Y. T. Chang, *Chem. Rev.*, 2012, **112**, 4391–4420.
- 5 Z. Liu, W. He and Z. Guo, *Chem. Soc. Rev.*, 2013, **42**, 1568–1600.
- 6 Y. M. Yang, Q. Zhao, W. Feng and S. Y. Li, *Chem. Rev.*, 2013, **113**, 192–270.
- 7 Y. Liua, J. Zhaob, Y. Wanga, J. Tian, X. Feic and H. Wanga, *J. Mol. Liq.*, 2017, **233**, 303–309.
- 8 J. Wu, W. Liu, J. Ge, H. Zhang and P. Wang, *Chem. Soc. Rev.*, 2011, **40**, 3483–3495.
- 9 A. Weller, *Naturwissenschaften*, 1955, **42**, 175–176.
- 10 J. Z. Zhao, S. M. Ji, Y. H. Chen, H. M. Guo and P. Yang, *Phys. Chem. Chem. Phys.*, 2012, **14**, 8803–8817.
- 11 C. Azarias, S. Budzak, A. D. Laurent, G. Ulrich and D. Jacquemin, *Chem. Sci.*, 2016, **7**, 3763–3774.
- 12 J. M. Berg and Y. Shi, *Science*, 1996, **271**, 1081–1085.
- 13 F. J. J. R. Da Silva and R. J. P. Williams, *The Biological Chemistry of the Elements*, Oxford University Press, 2nd edn, New York, 2001.
- 14 Y. Chen, K. Y. Han and Y. Liu, *Bioorg. Med. Chem.*, 2007, **15**, 4537–4542.
- 15 K. Komatsu, K. Kikuchi, H. Kojima, Y. Urano and T. Nagano, *J. Am. Chem. Soc.*, 2005, **127**(29), 10197–10204.
- 16 B. L. Vallee and K. H. Falchuk, *Physiol. Rev.*, 1993, **73**, 79–118.
- 17 C. B. Freddari, P. Fattoretti, T. Casoli, G. D. Stefano, B. Giorgetti and M. Ballelli, *Exp. Gerontol.*, 2008, **43**, 389–393.
- 18 N. P. Pavletich and C. O. Pabo, *Science*, 1991, **252**, 809–817.
- 19 C. O. Pabo and R. T. Sauer, *Annu. Rev. Biochem.*, 1992, **61**, 1053–1095.
- 20 K. A. McCall, C. C. Huang and C. A. Fierke, *J. Nutr.*, 2000, **130**, 1437S–1446S.
- 21 K. Jobe, C. H. Brennan, M. Motevalli, S. M. Goldup and M. Watkinson, *Chem. Commun.*, 2011, **37**, 6036–6038.
- 22 M. Ghosh, A. Ghosh, S. Ta, J. Matalobos and D. Das, *ChemistrySelect*, 2017, **2**, 7426–7431.
- 23 J. Quarterman, C. F. Mills and W. R. Humphries, *Biochem. Biophys. Res. Commun.*, 1966, **25**, 354–358.
- 24 E. U. Akkaya, M. E. Huston and A. W. Czarnik, *J. Am. Chem. Soc.*, 1990, **112**, 3590–3593.
- 25 D. A. Pearce, N. Jotterand, I. S. Carrico and B. Imperiali, *J. Am. Chem. Soc.*, 2001, **123**, 5160–5161.
- 26 Z. Xu, X. Liu, J. Pan and D. R. Spring, *Chem. Commun.*, 2012, **48**, 4764–4766.
- 27 J. Jiang, H. Jiang, X. Tang, L. Yang, W. Dou, W. Liu, R. Fang and W. Liu, *Dalton Trans.*, 2011, **40**, 6367–6370.
- 28 Y. Xu, J. Meng, L. Meng, Y. Dong, Y. Cheng and C. Zhu, *Chem.–Eur. J.*, 2010, **16**, 12898–12903.
- 29 L. Salmon, P. Thuery, E. Riviere and M. Ephritikhine, *Inorg. Chem.*, 2006, **45**, 83–93.
- 30 D. M. Epstein, S. Choudhary, M. R. Churchill, K. M. Keil, A. V. Eliseev and J. R. Morrow, *Inorg. Chem.*, 2001, **40**, 1591–1596.
- 31 B. Kumari, S. Lohar, M. Ghosh, S. Ta, A. Sengupta, P. P. Banerjee, A. Chattopadhyay and D. Das, *J. Fluoresc.*, 2016, **26**(1), 87–103.
- 32 R. E. Sturgeon, S. S. Berman, A. Desaulniers and D. S. Russell, *Anal. Chem.*, 1979, **14**, 2364–2369.
- 33 K. Aich, S. Goswami, S. Das and C. D. Mukhopadhyay, *RSC Adv.*, 2015, **5**, 31189–31194.
- 34 J. J. Lee, S. A. Lee, H. Kim, L. Nguyen, I. Noh and C. Kim, *RSC Adv.*, 2015, **5**, 41905–41913.
- 35 A. M. Hessels and M. Merckx, *Metallomics*, 2015, **7**, 258–266.
- 36 P. K. Mehta, E. T. Oh, H. J. Park and K. H. Lee, *Sens. Actuators, B*, 2017, **245**, 996–1003.
- 37 M. E. Shirbhate, Y. Jeong, G. Ko, G. Baek, G. Kim, Y. U. Kwon, K. M. Kim and J. Yoon, *Dyes Pigm.*, 2019, **167**, 29–35.
- 38 S. Pramanik, V. Bhalla and M. Kumar, *New J. Chem.*, 2017, **41**, 4806–4813.
- 39 M. Mariyappan, N. Malini, J. Sivamani, G. Sivaraman, M. Harikrishnan, S. Murugesan and A. Siva, *J. Fluoresc.*, 2019, **29**, 737–749.
- 40 S. Sinha, B. Chowdhury, N. N. Adarsh and P. Ghosh, *Dalton Trans.*, 2018, **47**, 6819–6830.
- 41 Y. Xu and Y. Pang, *Dalton Trans.*, 2011, **40**, 1503–1509.
- 42 S. Goswami, A. Manna, S. Paul, A. K. Maity, P. Saha, C. K. Quah and H. K. Fun, *RSC Adv.*, 2014, **4**, 34572–34576.
- 43 M. C. Burla, R. Caliendo, M. Camalli, B. Carrozzini, G. L. Casciarano, L. De Caro, C. Giacobozzo, G. Polidori and R. Spagna, *J. Appl. Crystallogr.*, 2005, **38**, 381–388.
- 44 G. M. Sheldrick, *Acta Crystallogr.*, 2008, **E64**, 112–122.
- 45 G. M. Sheldrick, *Acta Crystallogr.*, 2015, **A71**, 3–8.
- 46 O. V. Dolomanov, L. J. Bourhis, R. J. Gildea, J. A. K. Howard and H. Puschmann, *J. Appl. Crystallogr.*, 2009, **42**, 339–341.
- 47 A. Ghosh, S. Ta, M. Ghosh, S. Karmakar, A. Banik, T. K. Dangar, S. K. Mukherjee and D. Das, *Dalton Trans.*, 2016, **45**, 599–606.
- 48 M. Ghosh, S. Ta, M. Banerjee, M. Mahiuddin, S. Khanra, S. K. Hira, P. P. Manna and D. Das, *J. Photochem. Photobiol., A*, 2018, **367**, 32–38.
- 49 T. G. Jo, J. J. Lee, E. Nam, K. H. Bok, M. H. Lim and C. Kim, *New J. Chem.*, 2016, **40**, 8918–8927.

